

# Neutrino viscosity and drag: impact on the magnetorotational instability in proto-neutron stars

J r me Guilet, Ewald M ller & Hans-Thomas Janka

*Max-Planck-Institut fur Astrophysik, Karl-Schwarzschild-Str. 1, D-85748 Garching, Germany  
Max Planck/Princeton Center for Plasma Physics*

9 October 2014

## ABSTRACT

The magneto-rotational instability (MRI) is a promising mechanism to amplify the magnetic field in fast rotating proto-neutron stars (PNS). The diffusion of neutrinos trapped in the proto-neutron star induces a transport of momentum, which can be modeled as a viscosity on length scales longer than the neutrino mean free path. This neutrino-viscosity can slow down the growth of MRI modes to such an extent that a minimum initial magnetic field strength of  $\gtrsim 10^{12}$  G is needed for the MRI to grow on a sufficiently short timescale to potentially affect the explosion. It is uncertain whether the magnetic field of fast rotating progenitor cores is strong enough to yield such an initial magnetic field in proto-neutron stars. At MRI wavelengths shorter than the neutrino mean free path, on the other hand, neutrino radiation does not act as a viscosity but rather induces a drag on the velocity with a damping rate independent of the wavelength. We perform a linear analysis of the MRI in this regime, and apply our analytical results to the proto-neutron star structure from a one-dimensional numerical simulation. We show that in the outer layers of the PNS, the MRI can grow from weak magnetic fields at wavelengths shorter than the neutrino mean free path, while deeper in the PNS MRI growth takes place in the viscous regime and requires a minimum magnetic field strength.

**Key words:** magnetohydrodynamics – stars: neutron – stars: rotation – supernovae: general

## 1 INTRODUCTION

The explosion mechanism of core collapse supernovae and in particular the role played by rotation and magnetic fields is still uncertain. The neutrino driven mechanism aided by multidimensional hydrodynamical instabilities may be responsible for explosions with normal energies of  $10^{50}$  –  $10^{51}$  erg, though robust explosions with sufficient energy have yet to be demonstrated by three-dimensional numerical simulations including all relevant physics (e.g. Hanke et al. 2013; Mezzacappa et al. 2014). A small fraction of core collapse supernovae, however, have much larger explosion energies of  $\sim 10^{52}$  erg (“hypernovae” or type Ic BL, e.g. Drout et al. 2011), which most likely require an additional energy reservoir beyond neutrinos. Scenarios relying on a combination of fast rotation and strong magnetic fields may be good candidates to explain such extreme explosions. The rotation energy contained in a neutron star rotating with a period of one millisecond (near break-up velocity) is indeed a sufficient energy reservoir, which could be efficiently tapped if strong magnetic fields of the order of  $\sim 10^{15}$  G are present. Axisymmetric simulations assuming both a strong poloidal magnetic field and fast differen-

tial rotation have for example demonstrated the possibility of magnetorotational explosions (LeBlanc & Wilson 1970; Bisnovatyi-Kogan et al. 1976; Mueller & Hillebrandt 1979; Symbalisty 1984; Moiseenko et al. 2006; Shibata et al. 2006; Burrows et al. 2007; Dessart et al. 2008; Takiwaki et al. 2009; Takiwaki & Kotake 2011), although it remains to be demonstrated whether the explosion energy can reach that of hypernova-like explosions. Such magnetorotational explosions are furthermore a potential site for the production of r-process elements (Winteler et al. 2012). Note, however, that the 3D dynamics of magneto-rotational explosions needs to be explored further, since M sta et al. (2014) showed that non-axisymmetric instabilities can disrupt the jet before it can launch an explosion.

Another way by which fast rotation and strong magnetic fields could impact supernovae explosions is through the delayed injection of energy due to the spin down of a fast rotating, highly magnetized neutron star (Kasen & Bildsten 2010; Woosley 2010), which has been invoked as an explanation of some superluminous supernovae like SN 2008 bi (Dessart et al. 2012; Nicholl et al. 2013; Inserra et al. 2013). The birth of such “millisecond magnetars” is furthermore

a potential central engine for long gamma-ray bursts (e.g. Duncan & Thompson 1992; Metzger et al. 2011).

The very fast rotation needed by the above scenarios (magnetorotational explosion, millisecond magnetars) may not be present in the core of stars following standard stellar evolution, as Heger et al. (2005) showed that magnetic torques can slow down the core rotation efficiently. However, Yoon & Langer (2005) and Woosley & Heger (2006) showed that the fastest rotating stars could follow a chemically homogeneous evolution, in which the core can retain enough angular momentum to form a neutron star rotating with milliseconds period.

The second crucial ingredient for powerful magnetorotational energy release is an extremely strong, large-scale poloidal magnetic field of the order of  $10^{15}$  G. The presence of such a strong magnetic field in some proto-neutron stars is suggested by the observation of the most strongly magnetized neutron stars called magnetars (Woods & Thompson 2006, and references therein). The origin of this strong magnetic field remains, however, uncertain. One hypothesis is a fossil field origin in which the magnetic flux is inherited from the progenitor star (Ferrario & Wickramasinghe 2006), but it is not clear whether this can explain the population of magnetars. Given the uncertainty of having a sufficiently strong magnetic field in the iron core, intense research has been undertaken on physical mechanisms that could amplify the magnetic field during core collapse (in addition to the compression due to magnetic flux conservation during the collapse). In non-rotating progenitors, the SASI and convection have been invoked as a source of turbulence giving rise to a small scale dynamo (Endeve et al. 2010, 2012; Obergaulinger & Janka 2011; Obergaulinger et al. 2014). An Alfvén surface has also been shown to be a potential site of Alfvén wave and therefore magnetic field amplification (Guilet et al. 2011). But the most promising mechanisms rely on the fast rotation to drive a dynamo in the convective region of the proto-neutron star (Thompson & Duncan 1993), or through the magnetorotational instability (hereafter MRI) (e.g. Balbus & Hawley 1991; Akiyama et al. 2003).

Since the suggestion by Akiyama et al. (2003) that the MRI could play an important role in core collapse supernovae, the MRI has been the subject of a number of studies in the context of supernovae with the use of linear analysis (Masada et al. 2006, 2007), local (or "semi-global") numerical simulations representing a small portion of the proto-neutron star (Obergaulinger et al. 2009; Masada et al. 2012), and two-dimensional global numerical simulations (Sawai et al. 2013; Sawai & Yamada 2014). Masada et al. (2007) showed that neutrino radiation in the diffusive regime has several effects on the MRI. On the one hand, neutrino thermal and lepton number diffusion alleviates the stabilizing effect of entropy and lepton number gradients in stably stratified regions of the proto-neutron star. On the other hand, neutrino viscosity slows down MRI growth if the initial magnetic field is weaker than a critical strength, which Masada et al. (2012) estimated to be  $\sim 3.5 \times 10^{12}$  G. As a consequence of neutrino viscosity, a minimum magnetic field is needed for the MRI to grow on a sufficiently short timescale to affect the explosion (Masada et al. 2012). In this paper, we revisit this issue by computing the neutrino viscosity for the conditions given by the output of

a one-dimensional numerical simulation. We find that the effect of neutrino viscosity is even more pronounced: MRI growth is slowed down if the magnetic field is weaker than  $10^{13} - 10^{14}$  G (depending on the rotation rate), and becomes too slow to affect the explosion below a minimum strength of  $\sim 10^{12}$  G (see Section 3.2). This may be a problem for the MRI since the initial magnetic field in the proto-neutron star is extremely uncertain and could well be below this minimum strength.

The description of the effect of neutrinos by a viscosity is however valid only at length scales longer than the neutrino mean free path. We will show that, in the outer parts of the proto-neutron star, the viscous prescription is not self-consistent because the MRI grows at wavelengths shorter than the neutrino mean free path. We therefore provide the first description of the effect of neutrinos on the growth of the MRI that is valid at wavelengths shorter than the neutrino mean free path (section 3.3). This allows us to show that in the outer parts of the proto-neutron star, the MRI can grow from initially very weak magnetic fields.

The paper is organized as follows. In Section 2, we describe the numerical model of protoneutron star (hereafter PNS) structure. In Section 3, we analyze the different regimes in which the MRI can grow: analytical predictions are obtained, which are then applied to the PNS model. In Section 4, we discuss and conclude on the relevant regime of MRI growth as a function of radius in the PNS and magnetic field strength.

## 2 PROTO-NEUTRON STAR MODEL

In order to estimate physical quantities relevant for the growth of the MRI, we use the result of a one-dimensional numerical simulation as a typical structure of the proto-neutron star (PNS). The calculations were performed with the code Prometheus-Vertex, which combines the hydrodynamics solver Prometheus (Fryxell et al. 1989) with the neutrino transport module Vertex (Rampp & Janka 2002). Vertex solves the energy-dependent moment equations with the use of a variable Eddington factor closure, and including an up-to-date set of neutrino interaction rates (e.g. Müller et al. 2012). General relativistic corrections are taken into account by means of an effective gravitational potential (Marek et al. 2006). The model considered hereafter simulates the evolution of the  $11.2 M_{\odot}$  progenitor of Woosley et al. (2002), using the high-density equation of state of Lattimer & Swesty (1991) with a nuclear incompressibility of  $K = 220$  MeV. The results presented in this paper were obtained using a single time frame at  $t = 170$  ms after bounce. The radial profiles of density (upper panel) and temperature (middle panel) at this (arbitrary) reference time are shown in Figure 1. The structure of the PNS evolves in time due to its contraction and energy and lepton emission. We have therefore performed the same analysis at other times between  $t = 50$  ms and  $t = 800$  ms after bounce, obtaining very similar results: the main difference is the radius of the proto-neutron star (which decreases from 70 km to about 20 km), as will be discussed in Section 4.

As a simplified representation of the rotation profiles obtained by Ott et al. (2006), we further assume that the equatorial plane of the proto-neutron star is rotating with

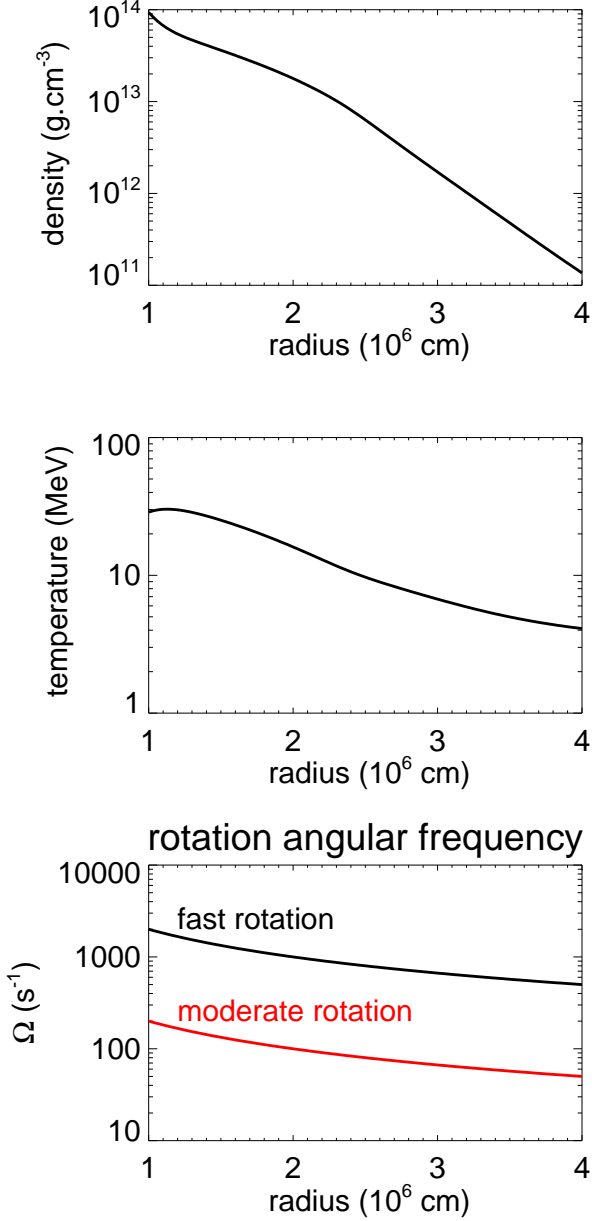


**Figure 1.** Structure of the proto-neutron star at time  $t = 170$  ms after bounce. Upper panel: Radial profile of the density. Middle panel: Radial profile of the temperature. Lower panel: radial profiles of rotation angular frequency defined in equations (1)-(2), with parameters  $\Omega_0 = 2000 \text{ s}^{-1}$  (black line) or  $\Omega_0 = 200 \text{ s}^{-1}$  (red line),  $q = 1$  and  $r_0 = 10 \text{ km}$ .

the following rotation profile<sup>1</sup>

$$\Omega = \Omega_0, \quad \text{if } r < r_0 \quad (1)$$

$$\Omega = \Omega_0 \left( \frac{r}{r_0} \right)^{-q}, \quad \text{if } r > r_0 \quad (2)$$

where  $\Omega_0$  is the angular frequency of the inner solidly rotat-

<sup>1</sup> since we restrict our analysis of MRI growth to the equatorial plane, we do not need to specify the angular dependence of the rotation frequency

ing core (at  $r < r_0$ ), and  $q$  is the power law index of the rotation profile assumed outside this inner core. Note that the MRI can grow only in regions where the angular frequency is decreasing outward, such that we only consider the outer region ( $r > r_0$ ) in the following analysis. As typical parameters, we have chosen  $q = 1$ ,  $r_0 = 10 \text{ km}$  and two different values of the angular frequency:  $\Omega_0 = 2000 \text{ s}^{-1}$  (fast rotation, black line in the lower panel of Figure 1) or  $\Omega_0 = 200 \text{ s}^{-1}$  (moderate rotation, red curve in the lower panel of Figure 1). Assuming shellular rotation, the total angular momentum contained in the PNS rotating with these angular frequency profiles would be:  $L = 4.7 \times 10^{48} \text{ g cm}^2 \text{ s}^{-1}$  (fast rotation), and  $L = 4.7 \times 10^{47} \text{ g cm}^2 \text{ s}^{-1}$  (moderate rotation). After cooling and contraction to a neutron star with a radius of 12 km and a moment of inertia of  $I = 1.5 \times 10^{45} \text{ g cm}^2$ , the neutron star would be rotating with a period (assuming angular momentum conservation):  $P = 2 \text{ ms}$  (fast rotation) and  $P = 20 \text{ ms}$  (moderate rotation). The fast rotation is comparable to the angular momentum of progenitors following the chemically homogeneous evolution (Yoon & Langer 2005; Woosley & Heger 2006), and may be thought of as representative of the scenario of millisecond magnetar formation (if magnetic field amplification to magnetar strength is indeed achieved), which is one of the central engines considered for gamma-ray bursts and hypernovae explosions. The moderately rotating model, on the other hand, is comparable to the progenitors of Heger et al. (2005) and is relevant to less extreme supernovae where rotation and magnetic field amplification may still play an important role.

Note that the PNS structure is taken from a one-dimensional numerical simulation of a non-rotating progenitor. Assuming a rotation profile is therefore not self-consistent, but should give the right order of magnitude as long as the rotation is not too extreme. This will be discussed in Section 4.

### 3 DIFFERENT REGIMES OF THE MAGNETOROTATIONAL INSTABILITY (MRI)

In this section, we obtain analytical estimates for the effect of neutrino radiation on the magnetorotational instability (MRI) growth in different regimes, corresponding to optically thick or optically thin neutrino transport at the MRI wavelength. In Section 3.1, we recall classical results on the linear growth of the MRI in ideal MHD (neglecting the effects of neutrino radiation). In section 3.2, we study the effect of neutrino viscosity on the growth of the MRI, which applies when the wavelength of the MRI exceeds the neutrino mean free path. In Section 3.3, we then consider the growth of the MRI at scales shorter than the neutrino mean free path.

In order to highlight these different regimes in a simple way, we have chosen to make a number of simplifying assumptions. First, we assume the initial magnetic field to be purely vertical, which is the most favorable configuration for MRI growth. The fastest growing MRI modes are then axisymmetric, with a purely vertical wave vector (e.g. Balbus & Hawley 1991), and we therefore make this assumption in the linear dispersion relations presented below. Second, we assume that the gas is incompressible, i.e. we assume

that the sound speed is much larger than the velocities and Alfvén speed (which should be reasonably well justified at least in the linear phase of the MRI) and neglect buoyancy effects due to the presence of entropy and composition gradients. Finally, we neglect the resistivity in all the scaling relations used to estimate the growth rate and wavelength of the MRI in the conditions prevailing inside the PNS. This assumption is justified by the very small value of the resistivity compared to the neutrino viscosity (by a factor of about  $10^{13}$ , e.g. Thompson & Duncan (1993); Masada et al. (2006)). For completeness, however, resistive effects are retained in the dispersion relations presented in Sections 3.2 and 3.3.

### 3.1 MRI in ideal MHD

Neglecting all diffusion coefficients as well as the effect of neutrino radiation, the dispersion relation of the axisymmetric MRI modes in the presence of a vertical magnetic field is (e.g. Balbus & Hawley 1991)

$$(\sigma^2 + k^2 v_A^2)^2 + \kappa^2 (\sigma^2 + k^2 v_A^2) - 4\Omega^2 k^2 v_A^2 = 0, \quad (3)$$

where  $\sigma$  is the growth rate,  $k$  is the wavenumber,  $v_A \equiv B/\sqrt{4\pi\rho}$  is the Alfvén velocity, and  $\kappa$  is the epicyclic frequency defined by  $\kappa^2 \equiv 2\frac{d\log r^2\Omega}{d\log r}$ . The analytical solution of this dispersion relation gives the growth rate and wavenumber of the fastest growing mode as

$$\sigma = \frac{q}{2}\Omega, \quad (4)$$

$$k = \sqrt{q(1-q/4)}\frac{\Omega}{v_A}, \quad (5)$$

where  $q \equiv -d\log\Omega/d\log r$  (consistent with the definition of the rotation profile in Section 2). The growth rate is independent of the magnetic field strength, and is extremely fast for rapid rotation

$$\sigma = 500 q \left(\frac{\Omega}{1000 \text{ s}^{-1}}\right) \text{ s}^{-1}. \quad (6)$$

The wavelength on the other hand is proportional to the magnetic field strength, such that weak magnetic fields lead to very short MRI wavelength in the ideal MHD case. Assuming  $q = 1$  leads to the following estimate for the wavelength

$$\lambda = 6 \left(\frac{B}{10^{12} \text{ G}}\right) \left(\frac{\rho}{10^{13} \text{ g cm}^{-3}}\right)^{-1/2} \left(\frac{\Omega}{1000 \text{ s}^{-1}}\right)^{-1} \text{ m}. \quad (7)$$

### 3.2 MRI in the presence of neutrino viscosity

#### 3.2.1 Neutrino viscosity in the proto-neutron star

Neutrinos present in a nascent protoneutron star can transport energy, lepton number and momentum. At length scales much larger than the mean free path of neutrinos, their transport can be described well by diffusive processes. In this regime, the transport of momentum by neutrinos gives rise to a viscosity  $\nu$ , which can be expressed as (van den Horn & van Weert 1984)

$$\nu = \frac{2}{15} \frac{E_\nu \langle l_\nu \rangle}{\rho c}, \quad (8)$$

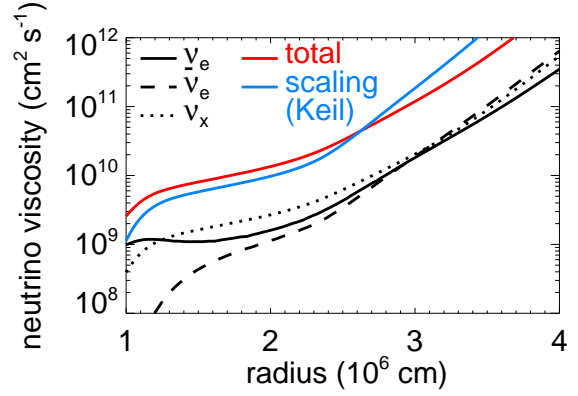


**Figure 2.** Radial profile of the neutrino viscosity, computed by applying equation (8) to the outputs of the numerical simulation. The solid black line corresponds to electron neutrinos, the dashed line to electron antineutrinos, the dotted line to heavy lepton neutrinos  $\nu_x$  (one representative species) and the solid red line to the total neutrino viscosity (i.e. the sum over the six neutrinos species). The blue solid line shows the approximate analytical estimate given by equation (10).

where  $c$  is the speed of light,  $E_\nu$  is the neutrino energy density, and  $\langle l_\nu \rangle$  is the neutrino mean free path averaged over energy following

$$\langle l_\nu \rangle \equiv \left( \int \frac{dE_\nu}{d\epsilon} l_\nu d\epsilon \right) / E_\nu, \quad (9)$$

with  $\epsilon$  the neutrino energy. Note that the numerical factor in equation (8) is different to that of van den Horn & van Weert (1984) due to our different definition of the neutrino mean free path averaged over energy.

We compute the viscosity caused by the neutrinos of different flavors by applying equation (8) to the output of the numerical simulation described in Section 2. The sum of the contributions from the 6 neutrino species gives the total neutrino viscosity, which varies between a few  $10^9 \text{ cm}^2 \text{ s}^{-1}$  near the inner boundary of the differentially rotating envelop and  $10^{12} \text{ cm}^2 \text{ s}^{-1}$  near the neutrinosphere (Figure 2). An approximate analytical expression for the neutrino viscosity as a function of density and temperature has been obtained by Keil et al. (1996) by considering six species of non-degenerate neutrinos in local thermodynamic equilibrium and assuming that the opacity comes only from scattering onto neutrons and protons in non-degenerate nuclear matter

$$\nu = 1.2 \times 10^{10} \left(\frac{T}{10 \text{ MeV}}\right)^2 \left(\frac{\rho}{10^{13} \text{ g cm}^{-3}}\right)^{-2} \text{ cm}^2 \text{ s}^{-1}. \quad (10)$$

This analytical formula is compared with the viscosity computed from the output of the numerical simulations in Figure 2. At radii  $13 \text{ km} < r < 23 \text{ km}$ , the analytical estimate reproduces the slope well and is in agreement with the numerical result within 30% (the difference is due to different prescriptions for opacity, and the neglect of degeneracy for electron neutrinos and antineutrinos). At  $r < 13 \text{ km}$ , high density effects like fermion blocking and nucleon correlation effects increase the mean free path in the numerical model but are neglected in equation (10), which therefore underestimates the viscosity. At  $r > 23 \text{ km}$ , the analytical estimate

increases faster than the value computed from the output of the simulation. This can be traced back to the fact that the heavy lepton neutrinos and electron antineutrinos are not perfectly in thermal equilibrium with the gas as assumed for equation (10).

It is interesting to compare this result to the literature. Masada et al. (2007, 2012) estimated a typical value of the neutrino viscosity  $\nu = 10^{10} \text{ cm}^2 \text{ s}^{-1}$  at a density of  $10^{12} \text{ g cm}^{-3}$ . This is about 10 times smaller than what we find at the same density (at a radius of  $\sim 32 \text{ km}$ ):  $\nu \sim 1 - 2 \times 10^{11} \text{ cm}^2 \text{ s}^{-1}$ . Thompson et al. (2005) have computed the neutrino viscosity due to different species of neutrinos (their Figure 5). The contribution from muon neutrinos varies between roughly a few times  $10^{10} \text{ cm}^2 \text{ s}^{-1}$  and  $10^{11} \text{ cm}^2 \text{ s}^{-1}$ , while our results show more variation between  $\sim 10^9 \text{ cm}^2 \text{ s}^{-1}$  and a few times  $\sim 10^{11} \text{ cm}^2 \text{ s}^{-1}$ . This difference might be due a different PNS structure (for example due to the different time (105 ms in their case) and equation of state).

In the next subsection, numerical estimates will use as fiducial values representative of a radius at 20 – 25 km from the center: a viscosity:  $\nu = 2 \times 10^{10} \text{ cm}^2 \text{ s}^{-1}$ , a density  $\rho = 10^{13} \text{ g cm}^{-3}$  and a rotation angular frequency  $\Omega = 1000 \text{ s}^{-1}$  (fast rotation).

### 3.2.2 Effect on the MRI

The dispersion relation of the magnetorotational instability in the presence of a viscosity  $\nu$  and a resistivity  $\eta$  can be written as (Lesur & Longaretti 2007; Pessah & Chan 2008; Masada & Sano 2008)

$$(\sigma_\nu \sigma_\eta + k^2 v_A^2)^2 + \kappa^2 (\sigma_\eta^2 + k^2 v_A^2) - 4\Omega^2 k^2 v_A^2 = 0, \quad (11)$$

where  $\sigma_\nu \equiv \sigma + k^2 \nu$  and  $\sigma_\eta \equiv \sigma + k^2 \eta$ . The effect of viscosity on the linear growth of the MRI is controlled by the Elsasser-like dimensionless number  $E_\nu \equiv \frac{v_A^2}{\nu \Omega}$  (e.g. Pessah & Chan 2008; Longaretti & Lesur 2010). For  $E_\nu < 1$ , viscosity affects significantly the growth of the MRI: as a result the growth rate is decreased, and the wavelength of the most unstable mode becomes longer. Typical conditions inside the protoneutron star lead to the following estimate of the Elsasser-like number for fast rotation at a radius  $\sim 20 - 25 \text{ km}$

$$E_\nu \sim 4 \times 10^{-4} \left( \frac{B}{10^{12} \text{ G}} \right)^2 \left( \frac{\rho}{10^{13} \text{ g cm}^{-3}} \right)^{-1} \left( \frac{\Omega}{1000 \text{ s}^{-1}} \right)^{-1} \times \left( \frac{\nu}{2 \times 10^{10} \text{ cm}^2 \text{ s}^{-1}} \right)^{-1}. \quad (12)$$

Viscosity therefore has a large effect on the linear growth of the MRI, unless the magnetic field is initially quite strong. The critical strength of the magnetic field below which viscous effects become important (at which  $E_\nu = 1$ ) is

$$B_{\text{visc}} = \sqrt{4\pi\rho\nu\Omega} \quad (13)$$

$$= 5 \times 10^{13} \left( \frac{\rho}{10^{13} \text{ g cm}^{-3}} \right)^{1/2} \left( \frac{\nu}{2 \times 10^{10} \text{ cm}^2 \text{ s}^{-1}} \right)^{1/2} \times \left( \frac{\Omega}{1000 \text{ s}^{-1}} \right)^{1/2} \text{ G}. \quad (14)$$

This critical magnetic field strength is shown as a function of radius in the PNS in Figure 3 (dashed lines). It decreases

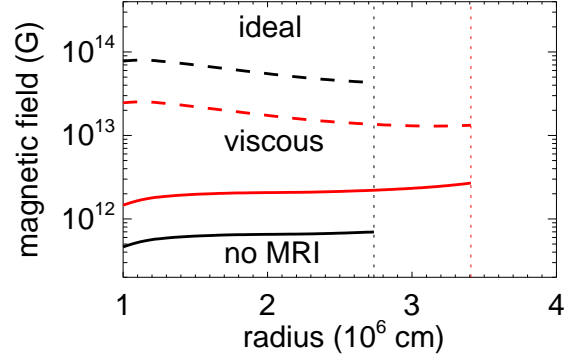


**Figure 3.** Radial profile of the critical magnetic field strengths that determine the regime of MRI growth. The dashed lines show the magnetic field strength  $B_{\text{visc}}$  (defined in equation (14)) below which viscous effects are important. The solid lines show the minimum magnetic field strength necessary for the MRI to grow at a growth rate faster than  $\sigma_{\text{min}} = 10 \text{ s}^{-1}$  (computed using equation (19)). The vertical dotted lines show the radius above which the viscous description breaks down because the mean free path of heavy lepton neutrinos becomes larger than the wavelength of the MRI. The two colors represent the two different normalizations of the rotation profile: fast rotation (black) and moderate rotation (red).

outward but only weakly because the effect of the decrease of density and angular frequency is partly compensated by the increase in neutrino viscosity. The initial magnetic field should be quite large so that MRI growth is not much affected by viscosity:  $B \gtrsim 5 \times 10^{13} - 10^{14} \text{ G}$  for fast rotation, and  $B \gtrsim 1 - 2 \times 10^{13} \text{ G}$  for moderate rotation. Note that these values are significantly larger than the one estimated by Masada et al. (2012) ( $\sim 3.5 \times 10^{12} \text{ G}$ ), which is due to the fact that the viscosity we have computed is significantly larger than the one they have estimated.

In order to describe the MRI growth in the viscous regime, useful analytical formulae can be obtained in the asymptotic limit  $E_\nu \ll 1$  (and neglecting the resistivity). The growth rate and wavenumber of the most unstable mode can then be expressed as (Pessah & Chan 2008; Masada & Sano 2008; Masada et al. 2012)

$$\sigma = \left( \frac{q E_\nu}{\tilde{\kappa}} \right)^{1/2} \Omega, \quad (15)$$

$$k = \left( \frac{\tilde{\kappa}}{\nu} \right)^{1/2}, \quad (16)$$

where  $\tilde{\kappa} \equiv \kappa/\Omega = \sqrt{2(2-q)}$  is the dimensionless epicyclic frequency. In contrast to the ideal MHD case, the wavelength of the fastest growing mode is independent of the magnetic field strength (because it is set by the viscous length scale), while the growth rate is proportional to the magnetic field strength: weak magnetic fields lead to slower growth. Using equations (15) and (16), we obtain the following estimates for the growth rate and wavelength of the fastest growing

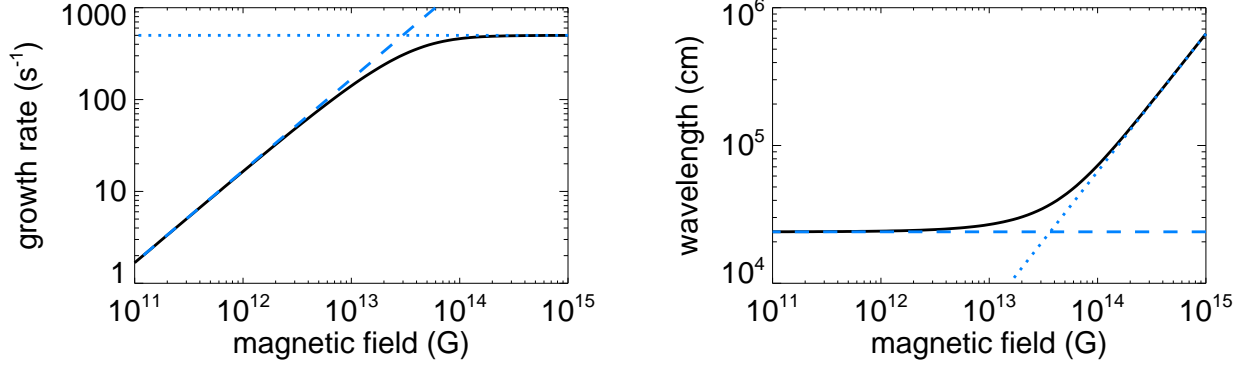


**Figure 4.** Growth rate (left) and wavelength (right) of the fastest growing MRI mode in the viscous regime as a function of the magnetic field strength for the following fiducial parameters:  $\nu = 2 \times 10^{10} \text{ cm}^2 \text{ s}^{-1}$ ,  $\rho = 10^{13} \text{ g cm}^{-3}$  and  $\Omega = 1000 \text{ s}^{-1}$ . The solid black line shows the numerical solution of the dispersion relation (equation 11). The dashed line shows the asymptotic behavior in the viscous regime ( $E_\nu \ll 1$ ), given by equations (15) and (16). The dotted line shows the asymptotic behavior in the ideal regime ( $E_\nu \gg 1$ ), given by equations (4) and (5).

MRI mode in the viscous regime

$$\sigma = 17 \left( \frac{B}{10^{12} \text{ G}} \right) \left( \frac{\rho}{10^{13} \text{ g cm}^{-3}} \right)^{-1/2} \times \left( \frac{\nu}{2 \times 10^{10} \text{ cm}^2 \text{ s}^{-1}} \right)^{-1/2} \left( \frac{\Omega}{1000 \text{ s}^{-1}} \right)^{1/2} \text{ s}^{-1}, \quad (17)$$

$$\lambda = 240 \left( \frac{\Omega}{1000 \text{ s}^{-1}} \right)^{-1/2} \left( \frac{\nu}{2 \times 10^{10} \text{ cm}^2 \text{ s}^{-1}} \right)^{1/2} \text{ m}. \quad (18)$$

Compared to the ideal regime described in Section 3.1, the wavelength is much longer and the growth much slower for a moderate magnetic field of  $10^{12} \text{ G}$ . The growth rate and wavelength of the most unstable MRI mode are shown in Figure 4 as a function of magnetic field strength (and the fiducial parameters for the viscosity, density and angular frequency representative of a radius at 20–25 km). The numerical solution of the dispersion relation (black solid line) is compared to the analytical solution in the asymptotic limits of ideal MRI  $E_\nu \gg 1$  (dotted blue lines, Section 3.1) and viscous MRI  $E_\nu \ll 1$  (dashed blue lines). The solution agrees within 20% with the ideal limit for  $E_\nu > 1.5$  or  $B > 6 \times 10^{13} \text{ G}$  (within 10% for  $E_\nu > 4$  or  $B > 10^{14} \text{ G}$ ), and with the viscous limit for  $E_\nu < 0.05$  or  $B < 10^{13} \text{ G}$  (within 10% for  $E_\nu < 10^{-2}$  or  $B < 5 \times 10^{12} \text{ G}$ ).

Figure 4 shows that, because of neutrino viscosity, the MRI requires a minimum magnetic field strength in order to grow fast enough to affect the explosion (as was already discussed by Masada et al. 2012). The minimum magnetic field necessary for the MRI to grow at a minimum growth rate  $\sigma_{\min}$  can be expressed using the viscous limit (equation 15)

$$\begin{aligned} B_{\min} &= \left( \frac{4\pi\rho\tilde{\kappa}\nu}{q\Omega} \right)^{1/2} \sigma_{\min}, \quad (19) \\ &= 6 \times 10^{11} \left( \frac{\sigma_{\min}}{10 \text{ s}^{-1}} \right) \left( \frac{\rho}{10^{13} \text{ g cm}^{-3}} \right)^{1/2} \\ &\quad \left( \frac{\nu}{2 \times 10^{10} \text{ cm}^2 \text{ s}^{-1}} \right)^{1/2} \left( \frac{\Omega}{1000 \text{ s}^{-1}} \right)^{-1/2} \text{ G}. \quad (20) \end{aligned}$$

Figure 3 shows this minimum magnetic field strength<sup>2</sup> as a function of radius, for  $\sigma_{\min} = 10 \text{ s}^{-1}$ . Similarly to the critical field  $B_{\text{visc}}$ , this minimum magnetic field strength  $B_{\min}$  depends very weakly on the radial position in the PNS (but this time slightly increasing outward due to the different scaling with  $\Omega$  and the same scaling with density and viscosity).  $B_{\min}$  is not that small ( $\sim 6 \times 10^{11} \text{ G}$  for fast rotation, and  $\sim 2 \times 10^{12} \text{ G}$  for moderate rotation), and we therefore conclude that neutrino viscosity sets a strong constraint on the initial magnetic field for the MRI to be able to grow on a sufficiently short timescale.

This constraint, however, only applies if the MRI wavelength is longer than the mean free path of neutrinos, which may not be the case everywhere in the PNS. Figure 5 shows the mean free path of the different species of neutrinos as a function of radius (the mean free path is averaged over neutrino energy following equation (9)). It increases by 4 to 5 orders of magnitudes from  $\langle l_\nu \rangle \sim 1 \text{ m}$  at  $r_0 = 10 \text{ km}$  to  $\langle l_\nu \rangle \gtrsim 10 \text{ km}$  near the PNS surface around 40 km. This dependence is approximately reproduced by the scaling  $l_\nu \propto \rho^{-1} T^{-2}$  (due to the main opacity contributions being proportional to the density and the square of the neutrino energy). The wavelength of the MRI in the viscous regime is independent of magnetic field strength (equation 17), and can be compared to the neutrino mean free path to check the consistency of the description (it is shown with the red curve in Figure 5 for the case of fast rotation). Because of the strong variation of the neutrino mean free path, the description of the effect of neutrino radiation as a viscosity is well justified deep inside the PNS, but

<sup>2</sup> This growth rate corresponds to an e-folding growth time of  $\sigma^{-1} = 100 \text{ ms}$  and is only a very rough estimate of the minimum growth rate needed for a significant magnetic field amplification. A significant amplification of the magnetic field by the MRI probably requires many e-folding times, and might actually take several seconds with this minimum growth rate. It is therefore possible that a dynamical effect of the MRI in the first second after shock bounce might require larger magnetic fields by a factor of a few.

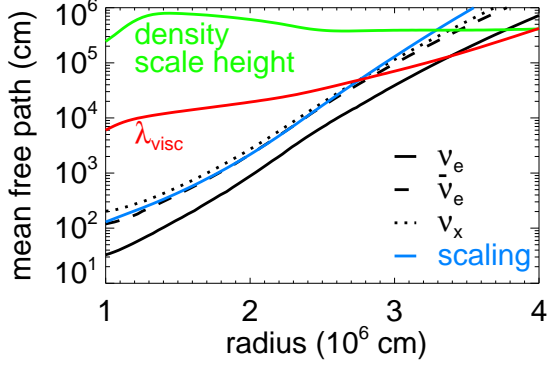


**Figure 5.** Radial profile of the neutrino mean free path. The solid black line corresponds to electron neutrinos, the dashed line to electron antineutrino and the dotted line to heavy lepton neutrinos  $\nu_x$ . The mean free paths are average over neutrino energy following equation (9). The blue line shows the scaling  $l_\nu = 10^4(\rho/10^{13} \text{ g cm}^{-3})^{-1}(T/10 \text{ MeV})^{-2}$ . For comparison, the density scale height is plotted with a green line, and the wavelength of the MRI in the viscous regime in red. For the latter we use the fast rotation profile defined in equations (1)-(2) with  $\Omega_0 = 2000 \text{ s}^{-1}$ ,  $q = 1$  and  $r_0 = 10 \text{ km}$ .

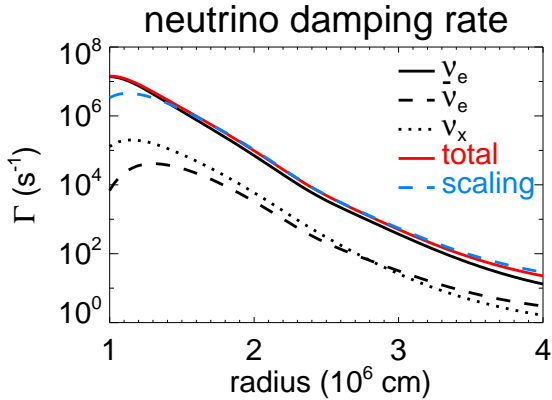


**Figure 6.** Radial profile of the neutrino drag damping rate computed according to equation (21). The solid black line corresponds to electron neutrinos, the dashed black line to electron antineutrinos, the dotted black line to heavy lepton neutrinos  $\nu_x$  (one representative species) and the solid red line to the total neutrino damping rate (i.e. the sum over the 6 neutrino species). Finally, the dashed blue line shows the scaling  $\Gamma = 6 \times 10^3 (T/10 \text{ MeV})^6$ .

breaks down at larger radii where the mean free path becomes longer than the MRI wavelength. This happens at radii  $\sim 27 \text{ km}$  for fast rotation and  $\sim 34 \text{ km}$  for moderate rotation, which are marked by the vertical dashed lines in Figure 3. At larger radii, the effect of neutrinos on the MRI cannot be described by a viscosity because neutrino transport begins to enter the non-diffusive regime.

### 3.3 MRI growth at wavelengths shorter than the neutrino mean free path

#### 3.3.1 Neutrino drag

At length scales shorter than the neutrino mean free path, the transport of momentum by neutrinos can no longer be described as a viscous process. This momentum transport does nevertheless damp velocity fluctuations. Agol & Krolik (1998) and Jedamzik et al. (1998) showed that, in this regime, radiation induces a drag on the velocity field which is independent of the wavenumber of the velocity fluctuations. This drag is caused by the Doppler effect due to fluid motion with respect to the background neutrino radiation field. This creates a neutrino flux in the rest frame of the fluid, which is responsible for the drag upon absorption or scattering of the neutrinos. The neutrino drag can be represented by an acceleration  $-\Gamma\delta\mathbf{u}$ , where  $\delta\mathbf{u}$  is the velocity perturbation and the damping rate  $\Gamma$  is given by

$$\Gamma \sim \frac{E_\nu \langle \kappa \rangle}{\rho c}, \quad (21)$$

where  $\langle \kappa \rangle$  is the neutrino opacity averaged over energy in the following way

$$\langle \kappa \rangle \equiv \left( \int \frac{dE_\nu}{d\epsilon} \kappa d\epsilon \right) / E_\nu. \quad (22)$$

Agol & Krolik (1998) obtained this result (with a numerical factor of 4/3) for photons subject to Thomson scattering, by performing a linearisation of the transport equation around an isotropic and steady radiation field, using a closure model that keeps terms up to the quadrupole and neglecting higher order (note that this is a higher order approximation than the so called Eddington closure). Jedamzik et al. (1998) found a similar result for neutrinos but did not derive the relevant numerical factor, which is most likely different from the one obtained by Agol & Krolik (1998) for photons.

Figure 6 shows the radial profile of the damping rate caused by the different neutrino species, obtained by evaluating equation (21) for the output of the numerical simulation. The contribution from electron neutrinos is dominant compared to that of other neutrino species because of their shorter mean free path. The damping rate decreases outward by about 6 orders of magnitudes from  $10^7 \text{ s}^{-1}$  at  $10 \text{ km}$  to  $10 \text{ s}^{-1}$  at  $40 \text{ km}$ . This can be explained by the scaling  $\Gamma \propto T^6$  (shown with a blue line in Figure 6), which results from the assumption of thermal equilibrium  $E_\nu \propto T^4$  and  $\kappa \propto \rho T^2$ . Thompson et al. (2005) obtained a neutrino damping rate of  $\Gamma \sim 50 \text{ s}^{-1}$  at a radius of  $50 \text{ km}$  (they do not show the values at smaller radii), which is of the same order of magnitude as what we obtain at the surface of the PNS.

Note that the damping rate  $\Gamma$  is related to the neutrino viscosity through  $\Gamma \sim 15\nu\langle\kappa\rangle/(2\langle l_\nu \rangle) \sim \nu/\langle l_\nu \rangle^2$ , i.e. it is (within a numerical factor) the rate at which fluctuations on the same scale as the neutrino mean free path would be damped by the neutrino viscosity. As a consequence the damping of fluctuations at scales shorter than the neutrino mean free path is less efficient by a factor  $\sim k^2\langle l_\nu \rangle^2$  (with  $k$  the wavenumber of the fluctuations) than what would be obtained by applying the viscous formalism at these scales. It is therefore conceivable that the MRI could grow on length

scales shorter than the neutrino mean free path even if the viscous formalism predicts the growth to be too slow.

### 3.3.2 Growth of the MRI in the presence of neutrino drag

In this section we study the growth of the MRI in the presence of neutrino drag, which is relevant to scales shorter than the neutrino mean free path. The equations of incompressible MHD in the shearing sheet approximation (Goldreich & Lynden-Bell 1965) are written as

$$\partial_t \mathbf{u} + \mathbf{u} \cdot \nabla \mathbf{u} = -\frac{1}{\rho} \nabla P + \frac{1}{\mu_0 \rho} (\nabla \times \mathbf{B}) \times \mathbf{B} - 2\boldsymbol{\Omega} \times \mathbf{u} + 2\Omega S x \mathbf{e}_x - \Gamma \delta \mathbf{u}, \quad (23)$$

$$\partial_t \mathbf{B} = \nabla \times (\mathbf{u} \times \mathbf{B}) + \eta \Delta \mathbf{B}, \quad (24)$$

$$\nabla \cdot \mathbf{u} = 0, \quad (25)$$

$$\nabla \cdot \mathbf{B} = 0, \quad (26)$$

where  $\boldsymbol{\Omega} \equiv \Omega \mathbf{e}_z$ ,  $S \equiv q\Omega$  is the shear rate, and  $\mathbf{e}_x, \mathbf{e}_y, \mathbf{e}_z$  are units vector in the radial, azimuthal and vertical directions (we restrict the analysis to the equatorial plane of the PNS).  $\delta \mathbf{u} \equiv \mathbf{u} - \mathbf{u}_0$  and  $\delta \mathbf{B} \equiv \mathbf{B} - \mathbf{B}_0$  are the velocity and magnetic field perturbations with respect to the stationary equilibrium solution  $\mathbf{B}_0 = B \mathbf{e}_z$ ,  $\mathbf{u}_0 = -q\Omega x \mathbf{e}_y$ . The only non-standard term in these equations is the neutrino drag  $-\Gamma \delta \mathbf{u}$  discussed in the preceding section. The velocity and magnetic field perturbations then follow the following set of equations

$$\sigma \delta u_x = \frac{B}{\mu_0 \rho} ik \delta B_x + 2\Omega \delta u_y - \Gamma \delta u_x, \quad (27)$$

$$\sigma \delta u_y - S \delta u_x = \frac{B}{\mu_0 \rho} ik \delta B_y - 2\Omega \delta u_x - \Gamma \delta u_y, \quad (28)$$

$$\delta u_z = 0, \quad (29)$$

$$\sigma \delta B_x = Bik \delta u_x - k^2 \eta \delta B_x, \quad (30)$$

$$\sigma \delta B_y = Bik \delta u_y - S \delta B_x - k^2 \eta \delta B_y, \quad (31)$$

$$\delta B_z = 0, \quad (32)$$

where the perturbations are assumed to have the following time and space dependence  $\delta A \propto e^{\sigma + ikz}$ , with  $\sigma$  being the growth rate of the modes, and  $k$  their vertical wave vector. Note that these equations are actually valid for any amplitude of the perturbations, as no linearisation had to be done to obtain them (just like the channel modes of the classical MRI are non-linear solutions in the incompressible limit (Goodman & Xu 1994)). These equations can be combined to obtain the dispersion relation of the MRI in this regime

$$(\sigma_v \sigma_\eta + k^2 v_A^2)^2 + \kappa^2 (\sigma_\eta^2 + k^2 v_A^2) - 4\Omega^2 k^2 v_A^2 = 0, \quad (33)$$

where we have defined

$$\sigma_v \equiv \sigma + \Gamma. \quad (34)$$

Note that the form of this equation is very similar to the dispersion relation in the viscous-resistive regime given by equation (11), the only difference being that  $\sigma_\nu = \sigma + k^2 \nu$  has been replaced by  $\sigma_v = \sigma + \Gamma$ . As we will show, the fact that the neutrino damping rate is independent of the wavenumber makes a big difference for the wavelength and growth rate of the fastest growing mode.

Figure 7 shows the growth rate and wavelength of the fastest growing MRI mode (the numerical solution of the dispersion relation for  $\eta = 0$  is shown with the solid black line)

as a function of the dimensionless parameter  $\Gamma/\Omega$  characterizing the effect of neutrino drag on the MRI. The growth of MRI channel modes is not much affected by the neutrino drag as long as  $\Gamma < \Omega$ . When the damping rate  $\Gamma$  is increased further, the growth rate of the MRI is reduced significantly while the wavelength of the fastest growing mode changes only slightly.

A useful analytical solution can be obtained in the asymptotic limit  $\Gamma \gg \Omega$  (and therefore  $\Gamma \gg \sigma$  since  $\sigma < \Omega$ ) and  $\eta = 0$ . In this limit, the dispersion relation reduces to

$$(\Gamma \sigma + k^2 v_A^2)^2 = k^2 v_A^2 (4\Omega^2 - \kappa^2). \quad (35)$$

The growth rate of the MRI as a function of vertical wavenumber is therefore

$$\sigma = \frac{k v_A}{\Gamma} \left( \sqrt{2q\Omega} - k v_A \right), \quad (36)$$

and the growth rate and wavenumber of the fastest growing mode are

$$\sigma = \frac{q}{2} \frac{\Omega^2}{\Gamma}, \quad (37)$$

and

$$k = \sqrt{q/2} \frac{\Omega}{v_A}, \quad (38)$$

respectively. The asymptotic limits  $\Gamma \gg \Omega$  (drag regime) and  $\Gamma \ll \Omega$  (i.e. the ideal regime described in Section 3.1) are compared to the full numerical solution in Figure 7. An agreement within 10% is obtained for  $\Gamma/\Omega < 0.2$  (ideal regime) and  $\Gamma/\Omega > 3$  (drag regime), and within 20% for  $\Gamma/\Omega < 0.4$  (ideal regime) and  $\Gamma/\Omega > 2$  (drag regime).

The analytical solution shows that compared to the ideal MHD case, the maximum growth rate is reduced by a factor  $\Gamma/\Omega$ . Importantly, and contrary to the viscous regime, the growth rate remains independent of the magnetic field strength. This comes from the fact that the neutrino drag is independent of the wavenumber, and as a consequence affects the MRI growing on a weak magnetic field (with short wavelength) in the same way as if it were growing on a stronger magnetic field (with longer wavelength). As a consequence, if the initial magnetic field is weak the MRI is more likely to grow in this regime than in the viscous regime (where the growth rate is proportional to magnetic field strength). The condition for the MRI to grow at a minimum growth rate  $\sigma_{\min}$  is independent of the magnetic field strength, and can be cast as an upper limit on the neutrino damping rate

$$\Gamma < q\Omega^2 / (2\sigma_{\min}). \quad (39)$$

Applying the analytical results of this section to the numerical model of the PNS allows one to compute the growth rate of the MRI as a function of radius in the PNS. The result is shown in Figure 8 for the two rotation profiles considered. Due to the large variation of the neutrino damping rate inside the PNS, different MRI growth regimes are encountered depending on the radius. Deep inside the PNS, the very large neutrino drag suppresses the growth of the MRI : this is due to the high temperature. Near the PNS surface on the contrary, the neutrino drag does not have much effect on the growth of the MRI (because  $\Gamma < \Omega$ ), which therefore occurs in the ideal regime described in Section 3.1. Finally, at intermediate radii, the neutrino drag has a significant impact on the MRI growth rate but still allows a sufficiently

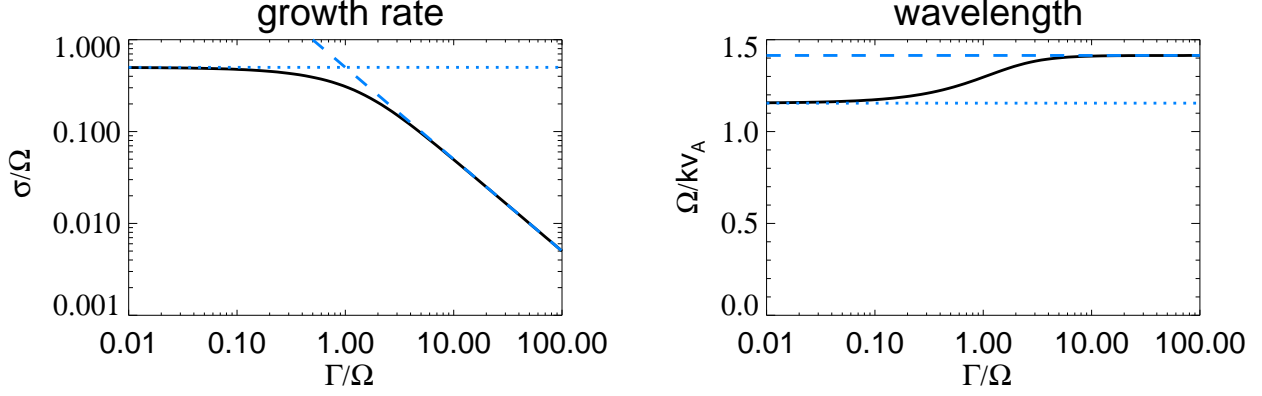


**Figure 7.** Growth rate (left) and wavelength (right) of the fastest growing MRI mode at scales shorter than the neutrino mean free path as a function of the damping rate  $\Gamma$  (assuming zero resistivity). The numerical solution of the dispersion relation (equation (33)) is shown with the solid black lines, the strongly damped limit  $\Gamma \gg \Omega$  (equations (37)-(38)) with dashed lines, and the ideal limit  $\Gamma = 0$  (Section 3.1) with dotted lines. All quantities are shown in a non-dimensional way:  $\Gamma$  and  $\sigma$  are normalized by the angular frequency  $\Omega$ , while  $\Omega/(k v_A)$  is a non-dimensional measure of the wavelength.

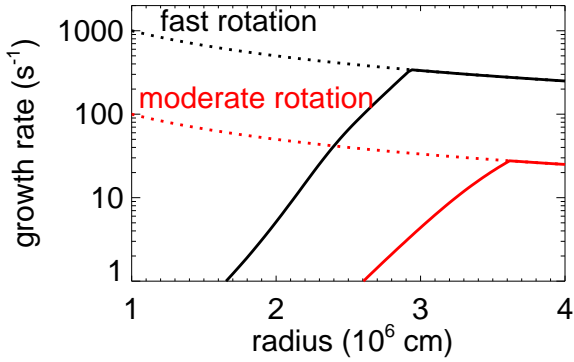


**Figure 8.** Radial profile of the maximum growth rate of the MRI at scales shorter than the neutrino mean free path. The growth rate (solid lines) is computed by applying equation (37) where  $\Gamma > \Omega$ , and equation (4) where  $\Gamma < \Omega$ . The dotted lines show the growth rate in the ideal MHD limit (equation (4)). The two colors represent the two different normalizations of the rotation profile: fast rotation (black) and moderate rotation (red).

fast growth (we call this the drag regime). The extent of the three different regimes depends on the rotation frequency : the MRI can grow in a larger portion of the PNS for fast rotation than for moderate rotation. Indeed if  $\Omega$  is larger the MRI can grow in the ideal regime for higher values of  $\Gamma$ , and therefore smaller radii. The extent of the drag regime also depends sensitively on  $\Omega$ : equation (37) shows that in this regime the MRI growth rate has a steeper dependence on the rotation rate ( $\sigma_{\max} \propto \Omega^2$ ) than in the ideal MHD case ( $\sigma_{\max} \propto \Omega$ ). This explains why the region where the MRI grows in the drag regime is less extended in the case of moderate rotation.

Finally, we should determine the condition for the formalism developed in this section to be self-consistent, i.e. that the wavelength of fastest MRI growth be shorter than the neutrino mean free path. As noted above, the wavelength of the fastest growing mode is of the same order of

magnitude as in the ideal MHD case, and is therefore proportional to the magnetic field strength. This is again in contrast to the viscous case, where the wavelength of the fastest growing mode is set by the viscosity and angular frequency (independently of the magnetic field strength). The results of this section are self-consistent if the wavelength of the fastest growing MRI mode is shorter than the neutrino mean free path. Using equation (38), this condition can be expressed as an upper limit on the magnetic field strength,

$$B < \sqrt{\rho q / 2\pi \Omega / \langle \kappa \rangle}, \quad (40)$$

because the relevant neutrino mean free path is the inverse of the opacity averaged over neutrino energy as defined by equation (22). Figure 9 shows this maximum magnetic field strength for consistency of MRI growth in the drag regime. It is quite weak ( $10^{10} - 10^{11}$  G) deep inside the PNS (where the MRI anyway does not grow efficiently due to the strong drag), and increases by two orders of magnitude toward the surface of the PNS reaching values of  $2 \times 10^{12}$  G for moderate rotation and  $2 \times 10^{13}$  G for fast rotation. This shows that the growth of the MRI at length scales shorter than the neutrino mean free path is relevant for weak to moderate initial magnetic fields in the outer parts of the PNS.

## 4 DISCUSSION AND CONCLUSION

In this paper we have studied the impact of neutrino radiation on the growth of the MRI. We have shown that, depending on the physical conditions, the MRI growth can occur in three different regimes:

- **Ideal regime** (orange color in Figure 10) : this is the classical MRI regime which applies when neutrino viscosity or drag are unimportant, i.e. if  $E_\nu > 1$  and  $\Gamma/\Omega < 1$ . The growth rate of the MRI is then a fraction of the angular frequency independently of the magnetic field strength, while the most unstable wavelength is proportional to the magnetic field strength.
- **Viscous regime** (dark blue color in Figure 10) : on length scales longer than the neutrino mean free path, neu-

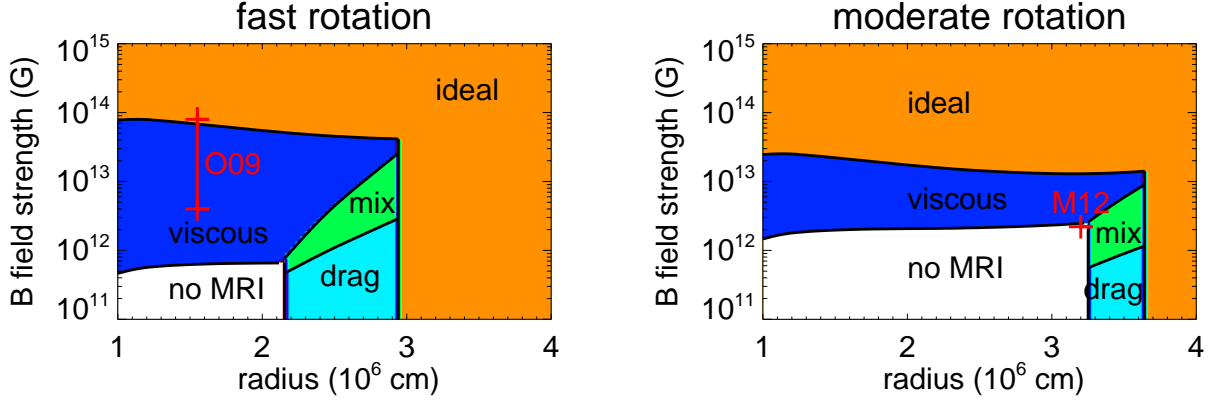


**Figure 10.** Different regimes of MRI growth as a function of radius and magnetic field strength in the case of fast rotation (left panel) and moderate rotation (right panel), for a PNS model at  $t = 170$  ms post-bounce. See text for a description of the different regimes. The parameter range used in the simulations by Obergaulinger et al. (2009) is shown in red on the left panel, and the parameters assumed by Masada et al. (2012) are shown with a red cross on the right panel.

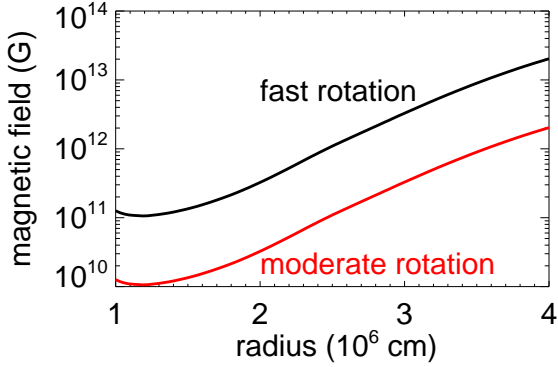


**Figure 9.** Magnetic field strength at which the wavelength of the fastest growing MRI mode equals the mean free path of electron neutrinos  $1/\langle\kappa\rangle$  (as defined by equation (22)): below this critical strength the formalism used in section 3.3 is self consistent. The two colors represent the two different normalizations of the rotation profile: fast rotation (black) and moderate rotation (red).

trino viscosity significantly affects the growth of the MRI if  $E_\nu < 1$ . The growth of the MRI is then slower and takes place at longer wavelength compared to the ideal regime. In the viscous regime, the wavelength of the most unstable mode is independent of magnetic field strength, while the growth rate is proportional to the magnetic field strength. As a result, a minimum magnetic field strength of  $\sim 10^{12}$  G is required for the MRI to grow on sufficiently short timescales.

- **Drag regime** (light blue color in Figure 10) : on length scales shorter than the neutrino mean free path, neutrino radiation exerts a drag on moving fluid elements. This drag has a significant impact on the MRI if the damping rate is larger than the rotation angular frequency ( $\Gamma > \Omega$ ). In this regime, the growth rate of the most unstable mode is independent of the magnetic field strength, but is reduced by a factor  $\Gamma/\Omega$  compared to the ideal regime. The wavelength of the most unstable mode is not much affected by the neutrino drag.

Figure 10 shows where in the parameter space these three regimes apply, as a function of radius and magnetic field strength for the two rotation profiles considered in this paper: fast rotation (left panel) and moderate rotation (right panel). Three regions in the proto-neutron can be distinguished:

- Deep inside the PNS, the neutrino mean free path is much shorter than the wavelength of the viscous MRI, and  $\Gamma \gg \Omega$ . In this case, the growth of the MRI at scales shorter than the mean free path is strongly suppressed, and the relevant MRI regime is the viscous MRI described in Section 3.2. The MRI can grow on sufficiently short timescales if the initial magnetic field is above a critical strength given by equation (19). Viscous effects become unimportant for strong magnetic fields above  $B_{\text{visc}}$  given by equation (14).

- At intermediate radii, the mean free path of neutrinos is still shorter than the wavelength of the viscous MRI, but  $\Gamma$  is not too large such that the MRI can also grow in the drag regime (i.e. equation (39) is verified). This is therefore an intermediate case where MRI growth can take place both in the viscous regime at wavelengths longer than the neutrino mean free path, and in the drag regime at length scales shorter than the mean free path. Since the growth rate in the viscous regime is proportional to the magnetic field strength, the growth is faster in the viscous regime above a critical magnetic field strength, which can be expressed as

$$B_{\text{visc-drag}} = \sqrt{q\pi\rho\nu\kappa} \frac{\Omega}{\Gamma}. \quad (41)$$

Below  $B_{\text{visc-drag}}$ , the growth is predicted to be faster in the drag regime. However, this regime is self-consistent only if the magnetic field strength is weaker than that given by equation (40) (the MRI wavelength is then shorter than the mean free path of electron neutrinos). In between these two critical strengths, the MRI growth should actually occur in a mixed regime (shown in green in Figure 10) where electron neutrinos are diffusing and thus induce a viscosity, while the other species make the transition to free streaming and exert a drag.

- Near the PNS surface, the viscous regime is irrelevant because the neutrino mean free path is longer than the wave-

length of the MRI. Furthermore, in this region the neutrino drag does not affect much the growth of the MRI because the damping rate is smaller than the angular frequency  $\Gamma < \Omega$ . As a consequence the MRI growth takes place in the ideal regime without much impact of neutrino radiation.

For the two rotation rates considered in this paper, the regimes of MRI growth have somewhat different locations in the parameter space. The region where the MRI cannot grow is more extended for moderate rotation than for fast rotation. The viscous and drag regimes are also less extended. For the ideal regime it is a bit more complicated: it extends to lower magnetic fields deep inside for slower rotation (because the wavelength is longer and the MRI is therefore less affected by viscosity), but weak field growth in the ideal regime can take place deeper inside the PNS for fast rotation (as explained in Section 3.3).

The results presented so far correspond to a single time frame at 170 ms after bounce. In order to study how the different MRI regimes are affected by the PNS contraction, we have performed the same analysis at two different times: 50 ms after bounce (at which time the PNS radius<sup>3</sup> is  $\sim 70$  km), and 800 ms after bounce (the PNS radius has then decreased to  $\sim 22$  km). Although the size and structure of the PNS is quite different at these different times, the results are strikingly similar: the location of the different MRI regimes is almost identical once rescaled to the size of the PNS, in particular with very similar values of  $B_{\min}$  and  $B_{\text{visc}}$  delimitating the viscous regime.

Note that the physical conditions inside the proto-neutron star (neutrino viscosity, neutrino damping rate etc.) have been estimated using a one dimensional numerical simulation of core collapse, which considered a non-rotating progenitor. The moderate rotation is expected to change the PNS structure in a negligible way because the ratio of centrifugal to gravitational forces is less than  $10^{-3}$  everywhere in the PNS. Fast rotation, on the other hand, should have a significant influence on the structure of the PNS, as the centrifugal force amounts to 4 to 8% of the gravitational force in the radius range considered. Rotational support is expected to lead to a more extended PNS and lower temperatures along the equatorial direction (Kotake et al. 2004; Ott et al. 2006). This would change quantitatively the results presented in this paper: for example the lower temperature would lead to smaller values of the neutrino damping rate, such that the MRI would be less affected by the neutrino drag in the outer envelop of the PNS. The centrifugal force also leads to an oblate PNS, and the MRI growth regime will therefore depend on the angular direction in addition to the radial dependence studied in this paper.

Numerical simulations of the MRI in core collapse supernovae have so far neglected the effects of neutrino radiation on the growth of the MRI (Obergaullinger et al. 2009; Masada et al. 2012; Sawai et al. 2013; Sawai & Yamada 2014). Our study shows that this assumption is reasonable for the exponential growth of the MRI only in a limited region of the parameter space, namely in the outer region of the proto-neutron star or deeper in the proto-neutron star but for quite strong initial magnetic fields

( $B \gtrsim 3 \times 10^{13} - 10^{14}$  G depending on the rotation rate<sup>4</sup>). If the initial magnetic field is not very strong, the growth of the MRI deep inside the PNS is strongly affected by neutrino viscosity. The effect of neutrinos should therefore be taken into account in numerical simulations either by adding a viscous or a drag term (depending on the regime of MRI growth) or by directly computing the neutrino transport and back reaction on the velocity field. In order to properly describe the effects of neutrinos on the MRI (viscosity and drag), a neutrino transport scheme should be multidimensional (i.e. not ray by ray) and should include velocity dependent terms.

Masada et al. (2012) performed local simulations of the MRI assuming a density  $\rho = 10^{12} \text{ g cm}^{-3}$  (this corresponds to a radius of  $\sim 32$  km in our PNS model), an initial magnetic field strength  $B = 2.2 \times 10^{12}$  G and an angular frequency  $\Omega = 100 \text{ s}^{-1}$ . This lies just at the limit between the viscous, mixed, and no-MRI regimes in the moderate rotation profile (their rotation is only slightly faster). We therefore conclude that neutrinos should be taken into account under these conditions, though the prescription to be applied (viscosity or drag) is not clear. Obergaullinger et al. (2009) considered a box localized at 15.5 km from the center of the PNS, with values at the center of the box of  $\rho = 2.5 \times 10^{13} \text{ g cm}^{-3}$ ,  $\Omega = 1900 \text{ s}^{-1}$  (i.e. close to the fast rotation profile we considered), and different values of the magnetic field strength varying between  $B = 4 \times 10^{12}$  G and  $B = 8 \times 10^{13}$  G. Under these conditions, the MRI is actually in the viscous regime and the neutrino viscosity should therefore be taken into account in the numerical simulation.

The large value of the neutrino viscosity has another important consequence: since the resistivity is quite small in comparison, this leads to a huge value of the magnetic Prandtl number (the ratio of viscosity to resistivity):  $\mathcal{P}_m \equiv \nu/\eta \sim 10^{13}$  (Thompson & Duncan 1993; Masada et al. 2007). Studies in the context of accretion discs have shown that the level of MRI turbulence is very sensitive to the magnetic Prandtl number, and that it generally increases with this number (e.g. Lesur & Longaretti 2007; Fromang et al. 2007; Longaretti & Lesur 2010). If viscosity is not explicitly taken into account in numerical simulations, numerical dissipation will give rise to a numerical magnetic Prandtl number which may depend on the numerical scheme but which should be of order unity (Fromang & Papaloizou 2007; Fromang et al. 2007). This is very far from the true regime, and could lead to underestimate strongly the final magnetic energy and stress. Numerical simulations taking explicitly into account neutrino viscosity will therefore be necessary to assess its influence on MRI saturation.

Let us now discuss the implications of our findings for the explosion mechanism of core collapse supernovae. We have shown that neutrino viscosity and drag have important consequences for the growth timescale of the MRI, which need to be taken into account. If the magnetic field is initially weak, the MRI growth can be suppressed by neutrino viscosity (if  $B \lesssim 10^{12}$  G in the PNS) or significantly slowed down (if  $B \lesssim 10^{13} - 10^{14}$  G). The most important finding

<sup>3</sup> The PNS radius is defined here as the radius at which the density equals  $10^{11} \text{ g cm}^{-3}$ .

<sup>4</sup> Note that this criterion only ensures that the linear growth rate is not much reduced by the viscosity, but the non-linear saturation of the MRI may still be affected by viscosity.

of this paper is probably that, even if the growth of the MRI from very weak magnetic fields is suppressed in the viscous regime deep inside the proto-neutron star, the MRI can grow on wavelengths shorter than the mean free path of neutrinos in the outer parts of the proto-neutron star. To have an impact on the explosion, it is probably more important that magnetic field amplification takes place in the outer parts of the PNS rather than in its inner parts. In this respect, our findings confirm that the growth of the MRI can be fast enough to play a role in the explosions of fast rotating progenitors. Which impact it has on the explosion will ultimately depend on the non-linear evolution and saturation of the MRI, which set the efficiency of magnetic field amplification. How this non-linear evolution is affected by the neutrino drag is currently unknown and should be the subject of future numerical studies.

In order to highlight the different regimes of MRI growth in a simple way, we have made a number of simplifying assumptions, which are discussed below. First, we have assumed the magnetic field to be purely poloidal. If the azimuthal magnetic field were much stronger than the poloidal one as obtained by Heger et al. (2005), the fastest growing perturbations would be non-axisymmetric (Masada et al. 2006). In a local analysis (like this article or Masada et al. (2006)), these shearing waves are only transiently growing typically during a few shear timescales, due to the fact that their radial wave vector increases linearly with time (and proportionally to the azimuthal wave vector). These transiently growing perturbations may play an important role in MRI turbulence and can be meaningfully studied using a non-modal approach (Squire & Bhattacharjee 2014b,a). It would be interesting to study their properties in the presence of neutrino drag. Second, we have neglected buoyancy effects, which can arise due to the presence of entropy and composition gradients. Buoyancy can however significantly impact MRI growth in stably stratified regions of the PNS (Balbus & Hawley 1994; Menou et al. 2004; Masada et al. 2006, 2007; Obergaulinger et al. 2009). In the neutrino diffusive regime, thermal and lepton number diffusion can alleviate the stabilizing effect of buoyancy on the MRI (Menou et al. 2004; Masada et al. 2007). Buoyancy effects on the MRI growth at wavelengths shorter than the neutrino mean free path are so far unknown and should be studied in the future, since they are relevant in the outer parts of the proto-neutron star.

## ACKNOWLEDGMENTS

We thank Florian Hanke for providing us with his simulation data. JG acknowledges support from the Max-Planck-Princeton Center for Plasma Physics.

## REFERENCES

Agol E., Krolik J., 1998, *ApJ*, 507, 304  
 Akiyama S., Wheeler J. C., Meier D. L., Lichtenstadt I., 2003, *ApJ*, 584, 954  
 Balbus S. A., Hawley J. F., 1991, *ApJ*, 376, 214  
 Balbus S. A., Hawley J. F., 1994, *MNRAS*, 266, 769

Bisnovatyi-Kogan G. S., Popov I. P., Samokhin A. A., 1976, *Ap&SS*, 41, 287  
 Burrows A., Dessart L., Livne E., Ott C. D., Murphy J., 2007, *ApJ*, 664, 416  
 Dessart L., Burrows A., Livne E., Ott C. D., 2008, *ApJL*, 673, L43  
 Dessart L., Hillier D. J., Waldman R., Livne E., Blondin S., 2012, *MNRAS*, 426, L76  
 Drout M. R., Soderberg A. M., Gal-Yam A., Cenko S. B., Fox D. B., Leonard D. C., Sand D. J., Moon D.-S., Arcavi I., Green Y., 2011, *ApJ*, 741, 97  
 Duncan R. C., Thompson C., 1992, *ApJL*, 392, L9  
 Endeve E., Cardall C. Y., Budiardja R. D., Beck S. W., Bejnood A., Toedte R. J., Mezzacappa A., Blondin J. M., 2012, *ApJ*, 751, 26  
 Endeve E., Cardall C. Y., Budiardja R. D., Mezzacappa A., 2010, *ApJ*, 713, 1219  
 Ferrario L., Wickramasinghe D., 2006, *MNRAS*, 367, 1323  
 Fromang S., Papaloizou J., 2007, *A&A*, 476, 1113  
 Fromang S., Papaloizou J., Lesur G., Heinemann T., 2007, *A&A*, 476, 1123  
 Fryxell B. A., Müller E., Arnett, D. 1989, Max-Planck-Institut für Astrophysik, Preprint, 449  
 Goldreich P., Lynden-Bell D., 1965, *MNRAS*, 130, 125  
 Goodman J., Xu G., 1994, *ApJ*, 432, 213  
 Guilet J., Foglizzo T., Fromang S., 2011, *ApJ*, 729, 71  
 Hanke F., Müller B., Wongwathanarat A., Marek A., Janka H.-T., 2013, *ApJ*, 770, 66  
 Heger A., Woosley S. E., Spruit H. C., 2005, *ApJ*, 626, 350  
 Inserra C., Smartt S. J., Jerkstrand A., et al. 2013, *ApJ*, 770, 128  
 Jedamzik K., Katalinić V., Olinto A. V., 1998, *Phys. Rev. D*, 57, 3264  
 Kasen D., Bildsten L., 2010, *ApJ*, 717, 245  
 Keil W., Janka H., Müller E., 1996, *ApJL*, 473, L111+  
 Kotake K., Sawai H., Yamada S., Sato K., 2004, *ApJ*, 608, 391  
 Lattimer J. M., Swesty F. D., 1991, *Nuclear Physics A*, 535, 331  
 LeBlanc J. M., Wilson J. R., 1970, *ApJ*, 161, 541  
 Lesur G., Longaretti P.-Y., 2007, *MNRAS*, 378, 1471  
 Longaretti P.-Y., Lesur G., 2010, *A&A*, 516, A51  
 Marek A., Dimmelmeier H., Janka H., Müller E., Buras R., 2006, *A&A*, 445, 273  
 Masada Y., Sano T., 2008, *ApJ*, 689, 1234  
 Masada Y., Sano T., Shibata K., 2007, *ApJ*, 655, 447  
 Masada Y., Sano T., Takabe H., 2006, *ApJ*, 641, 447  
 Masada Y., Takiwaki T., Kotake K., Sano T., 2012, *ApJ*, 759, 110  
 Menou K., Balbus S. A., Spruit H. C., 2004, *ApJ*, 607, 564  
 Metzger B. D., Giannios D., Thompson T. A., Bucciantini N., Quataert E., 2011, *MNRAS*, 413, 2031  
 Mezzacappa A., Bruenn S. W., Lentz E. J., Hix W. R., Bronson Messer O. E., Harris J. A., Lingerfelt E. J., Endeve E., Yakunin K. N., Blondin J. M., Marronetti P., 2014, *ArXiv e-prints*  
 Moiseenko S. G., Bisnovatyi-Kogan G. S., Ardeljan N. V., 2006, *MNRAS*, 370, 501  
 Mösta P., Richers S., Ott C. D., Haas R., Piro A. L., Boydston K., Abdikamalov E., Reisswig C., Schnetter E., 2014, *ApJL*, 785, L29  
 Mueller E., Hillebrandt W., 1979, *A&A*, 80, 147

- Müller B., Janka H.-T., Marek A., 2012, *ApJ*, 756, 84
- Nicholl M., Smartt S. J., Jerkstrand A., et al. 2013, *Nature*, 502, 346
- Obergaulinger M., Cerdá-Durán P., Müller E., Aloy M. A., 2009, *A&A*, 498, 241
- Obergaulinger M., Janka H.-T., 2011, preprint (arXiv:1101.1198)
- Obergaulinger M., Janka T., Aloy Toras M. A., 2014, preprint (arXiv:1405.7466)
- Ott C. D., Burrows A., Thompson T. A., Livne E., Walder R., 2006, *ApJS*, 164, 130
- Pessah M. E., Chan C.-k., 2008, *ApJ*, 684, 498
- Rampp M., Janka H.-T., 2002, *A&A*, 396, 361
- Sawai H., Yamada S., 2014, *ApJL*, 784, L10
- Sawai H., Yamada S., Suzuki H., 2013, *ApJL*, 770, L19
- Shibata M., Liu Y. T., Shapiro S. L., Stephens B. C., 2006, *Phys. Rev. D*, 74, 104026
- Squire J., Bhattacharjee A., 2014a, preprint (arXiv:1407.4742)
- Squire J., Bhattacharjee A., 2014b, *Physical Review Letters*, 113, 025006
- Symbalisty E. M. D., 1984, *ApJ*, 285, 729
- Takiwaki T., Kotake K., 2011, *ApJ*, 743, 30
- Takiwaki T., Kotake K., Sato K., 2009, *ApJ*, 691, 1360
- Thompson C., Duncan R. C., 1993, *ApJ*, 408, 194
- Thompson T. A., Quataert E., Burrows A., 2005, *ApJ*, 620, 861
- van den Horn L. J., van Weert C. G., 1984, *A&A*, 136, 74
- Winteler C., Käppeli R., Perego A., Arcones A., Vasset N., Nishimura N., Liebendörfer M., Thielemann F.-K., 2012, *ApJL*, 750, L22
- Woods P. M., Thompson C., 2006, *Soft gamma repeaters and anomalous X-ray pulsars: magnetar candidates*. pp 547–586
- Woosley S. E., 2010, *ApJL*, 719, L204
- Woosley S. E., Heger A., 2006, *ApJ*, 637, 914
- Woosley S. E., Heger A., Weaver T. A., 2002, *Reviews of Modern Physics*, 74, 1015
- Yoon S.-C., Langer N., 2005, *A&A*, 443, 643

This paper has been typeset from a  $\text{\LaTeX}$  file prepared by the author.